

LidarDM: Generative LiDAR Simulation in a Generated World

Vlas Zyrianov¹, Henry Che¹, Zhijian Liu², and Shenlong Wang¹ 

¹ University of Illinois, Urbana-Champaign, IL, USA

{vlasz2,hungdc2,shenlong}@illinois.edu

² Massachusetts Institute of Technology, MA, USA

zhijian@mit.edu

www.zyrianov.org/lidardm

Abstract. We present LidarDM, a novel LiDAR generative model capable of producing *realistic*, *layout-aware*, *physically plausible*, and *temporally coherent* LiDAR videos. LidarDM stands out with two unprecedented capabilities in LiDAR generative modeling: (i) LiDAR generation guided by driving scenarios, offering significant potential for autonomous driving simulations, and (ii) 4D LiDAR point cloud generation, enabling the creation of realistic and temporally coherent sequences. At the heart of our model is a novel integrated 4D world generation framework. Specifically, we employ latent diffusion models to generate the 3D scene, combine it with dynamic actors to form the underlying 4D world, and subsequently produce realistic sensory observations within this virtual environment. Our experiments indicate that our approach outperforms competing algorithms in realism, temporal coherency, and layout consistency. We additionally show that LidarDM can be used as a generative world model simulator for training and testing perception models.

Keywords: LiDAR Generation · Scene Generation · Self-driving

1 Introduction

Generative models have become notable in understanding data distributions and content creation, *e.g.* in image and video generation [10, 33, 52–55], 3D object generation [10, 19, 38, 52], compression [5, 29, 68], and editing [37, 47]. Generative models also show significant promise for simulation [6, 11, 18, 34, 46, 60, 64, 66, 76, 82], capable of creating realistic scenarios and their associated sensory data for training and evaluating safety-critical embodied agents, such as in robotics and autonomous vehicles, without the need of expensive manual modeling of the real world. These capabilities are crucial for applications that rely on extensive closed-loop training or scenario testing.

While advancements in conditional image and video generation [15, 27, 35, 44] have been remarkable, the specific task of generatively creating scenario-specific,

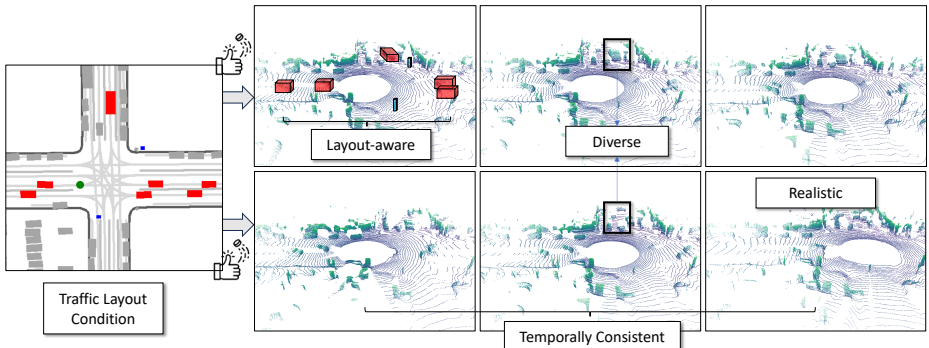


Fig. 1: We present LidarDM, a novel 4D LiDAR generative model. Our generated LiDAR videos simultaneously enjoy the benefits of being realistic, layout-conditioning, physically plausible, diverse, and temporally coherent.

realistic LiDAR point cloud sequences for autonomous driving application remains under-explored. Current LiDAR generation methods fall into two broad categories, each of which suffers from specific challenges:

1. *LiDAR generative modeling methods* [8, 72, 79, 83] are currently limited to single-frame generation and do not provide the means for semantic controllability and temporal consistency.
2. *LiDAR resimulation* [14, 17, 46, 65, 67, 74] depends heavily on user-created or real-world collected assets. This induces a high operational cost, restricts diversity, and limits broader applicability.

To address these challenges, we propose LidarDM (Lidar Diffusion Model), which creates *realistic*, *layout-aware*, *physically plausible*, and *temporally coherent* LiDAR videos. We explore two novel capabilities that have not been previously addressed: (i) LiDAR synthesis guided by driving scenarios, which holds immense potential for simulation in autonomous driving, and (ii) 4D LiDAR point cloud synthesis aimed at producing realistic and temporally coherent sequences of labeled LiDAR point clouds. Our key insight to achieving these goals lies in first generating and composing the underlying 4D world and then creating realistic sensory observations within this virtual environment. To achieve this, we integrate existing 3D object generation approaches to create dynamic actors and develop a novel approach for large-scale 3D scene generation based on the latent diffusion model. This method produces realistic and diverse 3D driving scenes from a coarse semantic layout, which to our knowledge, is one of the first of its kind. We apply trajectory generation to create dynamic effects while ensuring authentic interactions among actors and between actors and the scene. Finally, we compose the 3D world at each time step and perform stochastic raycasting simulation to produce the final 4D LiDAR sequence. As shown in Fig. 1, our generated results are diverse, align with the layout conditions, and are both realistic and temporally coherent.

Our experimental results demonstrate that individual frames generated by LidarDM exhibit *realism* and *diversity*, with performance that is on-par with

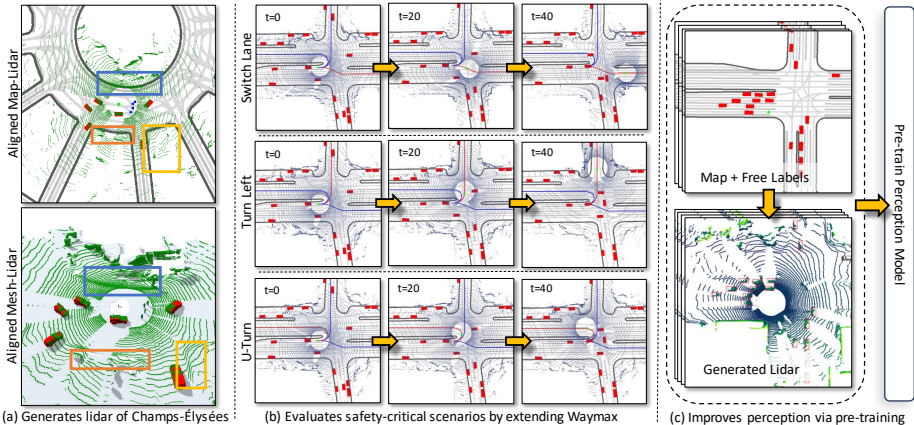


Fig. 2: Applications of LidarDM: (a) generating LiDAR that aligns well with the map (color boxes highlight the consistency between the lidar and the map) without 3D capturing or modeling; (b) providing sensor data for an existing traffic simulator (Waymax [20]), enabling safety-critical scenarios evaluation from pure sensor data; (c) generate large volume LiDAR data with controllable obstacles locations (treated as ground-truth labels, which are free to obtain) to improve perception models via pre-training without expensive data capturing and labelling.

state-of-the-art techniques in unconditional single-frame LiDAR point cloud generation. Moreover, we show that LidarDM can produce LiDAR videos that maintain *temporal coherency*, outperforming a robust stable diffusion sensor generation baseline. To our knowledge, this is the **first LiDAR generative method** with this capability. We further demonstrate LidarDM’s *conditional generation* by showing that the generated LiDAR matches well with ground-truth LiDAR on matching map conditions. Lastly, we illustrate that the data generated by LidarDM exhibit a *minimal domain gap* when tested with perception modules trained on real data and can also be used to augment training data to significantly boost the performance of 3D detectors. This gives premise for using generative LiDAR models to create realistic and controllable simulations for training and testing driving models (Please refer to Sec. 2 and Fig. 2 for detailed applications of LidarDM).

2 Related Works

LiDAR Simulation. Realistic LiDAR sensor simulation is crucial for robotics and self-driving vehicle training and testing. Traditional LiDAR generation methods use raycasting-based physical approaches. Simulators like CARLA [14] and AirSim [59] create environments with static (buildings, trees, street lights) and dynamic objects (cars, bicycles, buses). In these settings, virtual LiDAR sensors are placed, casting rays to calculate depth through ray-triangle intersections. Such approaches are simple and easy to integrate, hence are widely used in robot simulation [4, 45]. Asset-based physical simulation methods for LiDAR face limitations in realism and scalability due to three key issues: the need for 3D assets,

which are costly and limit variations; further, they also face challenges in closing the sim2real gap for both asset design and physics simulation.

Recent research attempts to address these shortcomings through data-driven approaches. LiDARSim [46] uses collected LiDAR sequences to reconstruct maps and dynamic assets. Subsequent works have improved asset reconstruction using neural fields-based approaches like NeRF [30, 67] or neural feature fields [74], and with automatic alignment [58], or with past LiDAR readings [30]. Additionally, realistic physics effects such as ray dropping [49] and snow [21] have also been modeled. However, constructing detailed 3D maps and objects from real-world sensor data is often costly and not scalable, typically requiring multiple passes over the same locations.

Our approach, unlike traditional LiDAR simulations, is purely generative, eliminating the need for man-made or reconstructed assets and allowing for easy creation of numerous virtual worlds. In Fig. 2 (a), we present a realistic generated LiDAR point cloud of Champs-Élysées from only a hand-crafted map layout (without any actual sensor data from France), which no re-simulation methods can achieve.

LiDAR Generation. Generative models provide a promising alternative for creating realistic LiDAR point clouds without reconstructing real-world environments. Early LiDAR generation work exploited the range image representation for LiDAR generation. The pioneering work by Caccia et al. [8] focused on using GANs and VAEs for unconditional generation and performing reconstruction tasks for noisy LiDAR readings. LiDARGen [83] showed that using a score-based diffusion model provides improved generative capability and can be used in downstream classifier-guided sampling tasks such as point cloud upsampling. The range image representation offers the benefit of physically accurate rendering at the cost of being ego-centric, rather than scene-centric. Recently, UltraLiDAR [72] proposed using a BEV voxel grid representation for LiDAR generation. Sampling is performed with a VQVAE [50] in a learned discrete latent space, ensuring a dense latent space. The BEV-centric representation provides the benefit of improved layout coherence and metrics, at the cost of not guaranteeing a physically accurate LiDAR sample. However, despite significant advancements, current generative models do not support conditioning on semantic layouts. This omission makes the generation process less controllable, reducing its practical applications. Additionally, a model ensuring temporal consistency in LiDAR video generation remains to be developed.

Unlike previous methods, our model addresses this challenge by (1) generalizing the task of LiDAR generation to geometry generation and data-driven ray casting in a novel field representation; (2) guiding generation with a BEV HD Map layout; and (3) allowing complete control over dynamic scene composition by adding generated 3D models and enabling free movement of the virtual LiDAR sensor within the frame. Fig. 2 (b) and (c), respectively, show that LiDARDM’s point cloud can provide realistic LiDAR information to an existing traffic simulator for autonomous driving’s safety-critical case evaluation thanks to its temporal consistency, and can improve perception accuracy (Sec. 4.5) thanks

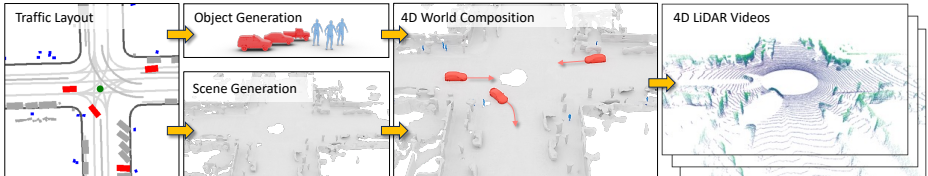


Fig. 3: Overview of the LidarDM: Given the input traffic layout at time $t = 0$, LidarDM begins by generating actors and the static scene. We then generate the motion of the actors and the egocar, and compose the underlying 4D world. Finally, a generative- and physics-based simulation is used to create realistic 4D sensor data.

to its full controllability of scenarios, which means ground-truth detection labels are free to obtain. These two important benefits cannot be achieved with any other LiDAR generative methods.

Diffusion Models. Our model builds upon the recent advancement in latent diffusion models. Directly applying diffusion models [24, 62] on data can be burdensome on the denoising network due to the issue of data sparsity. Latent diffusion alleviates this issue by performing the diffusion process on a dense latent space of an autoencoder. Models such as stable diffusion [54], stable diffusion XL [51], and MaskGIT [9] have championed latent diffusion as a highly effective technique for generative modeling.

Sampling: A key challenge in diffusion-based modeling lies in selecting the sampling procedure. Early methods utilized Langevin dynamics or ancestral sampling. Recent sampling quality and speed improvements have come from deterministic non-Markovian techniques like DDIM [61] and PNDM [40]. Additionally, the differential equation interpretation of diffusion models has led to the development of samplers like Euler [32] and DPM-Solver [43]. We empirically find Euler works well in practice for our model.

Conditioning: Various strategies have been devised to integrate conditions into the diffusion model generation process. Classifier-based guidance (or posterior sampling) [47, 62, 83] utilizes the gradient of a classifier to enhance the model’s score function. Classifier-free guidance [23] offers a method for training and sampling class-conditioned diffusion models. Controlnet [80] introduces a technique for adding controllability to a pre-trained diffusion model through a class-conditioned hypernetwork. Our approach leverages classifier-free guidance.

In diffusion-based *video generation* [22, 25, 31, 70, 71, 73], maintaining consistency is a central challenge. Various approaches have been proposed, leveraging motion modeling, interpolation, or batch sampling to enhance consistency. Our model is the first to focus on LiDAR video generation. Unlike other methods, our technique capitalizes on LiDAR’s unique attribute of underlying 3D world alignment, significantly improving temporal consistency.

3 Layout-Guided LiDAR Video Generation

Our goal is to create a realistic, physically plausible, and temporally consistent LiDAR sequence that enables a free viewpoint based on a given bird’s eye

view semantic layout in a purely generative manner without relying on any pre-collected assets like 3D maps. To our knowledge, this is the first solution of its kind, addressing layout-conditioned LiDAR generation and LiDAR video generation. The key to achieving this lies in first generating and composing the underlying 3D world, followed by using generative simulation to create realistic sensory observations. We begin by formulating the generation as a joint 4D scene generation task (Sec. 3.1). Next, we discuss leveraging 3D diffusion models to create static and dynamic elements, ensuring their faithful interaction (Sec. 3.2). Finally, a sensor generation procedure is executed to produce the final LiDAR video (Sec. 3.3). Fig. 3 depicts the overview of our method.

3.1 Problem Formulation

Formally, given an input layout $\mathcal{I} \in \mathbb{R}^{L \times W \times M}$ representing traffic elements from a bird’s eye view (where L , W , and M are length, width, and map classes, respectively), our goal is to generate a LiDAR point cloud video $\mathcal{X} = \{\mathbf{x}_t\}$, with each $\mathbf{x}_t \in \mathbb{R}^{N \times 3}$ being a point cloud at frame t with \mathbf{x}_0 matching the input layout. This conditional generation setting offers full controllability, and hence lays the foundation for a practical asset-free simulator. Note that in the absence of a map, our approach defaults to unconditional generation.

4D World Representation. Our key technical innovation to address the challenge lies in jointly modeling the generation of underlying 4D world together sensor generation. We define the world scene representation as $\mathcal{W} = \{\mathbf{s}, \{\mathbf{o}_i\}_{i=0}^N\}$, where \mathbf{s} represents a static scene geometry and $\mathbf{o}_0, \dots, \mathbf{o}_N$ are dynamic objects. Both are represented in the form of an occupancy grid. To model dynamics, we additionally consider the actions of these dynamic objects in the form of trajectories $\mathcal{P} = \{\boldsymbol{\tau}_0, \dots, \boldsymbol{\tau}_T\}$, with $\boldsymbol{\tau}_t = \{\boldsymbol{\xi}_{\text{ego}}, \{\boldsymbol{\xi}_{i,t}\}_{i=0}^N\}$ representing the pose of actor i at time t as well as egocar pose $\boldsymbol{\xi}_{\text{ego}}$. The pose for rigid objects and the egocar lies in the $\text{SE}(3)$ space, while for articulated objects like pedestrians, it is represented as a kinematic chain. A composed scene represent the states of the world at t , incorporating the poses of the ego car and dynamic objects at time t , is denoted by $\mathcal{W}_t = \pi(\mathcal{W}, \boldsymbol{\tau}_t)$, where π is a composition operator applying transformations to each actor.

4D World and LiDAR Generation. To ensure realism and consistency over time and between the world and sensory readings, we formulate the generation task as a sampling problem from the joint distribution $p(\mathcal{X}, \mathcal{P}, \mathcal{W} | \mathcal{I})$. Directly modeling and sampling the joint distribution, however, is challenging as it involves estimating a distribution across multiple data modalities (e.g., car trajectories, scene layouts, sensor noise, etc.). To tackle this, we factorize the joint distribution $p(\mathcal{X}, \mathcal{P}, \mathcal{W} | \mathcal{I})$ as follows:

$$p(\mathbf{s} | \mathcal{I}) \cdot \underbrace{\prod_i p(\mathbf{o}_i | \mathcal{I})}_{\text{3D scene and object gen}} \cdot \underbrace{\prod_t p(\boldsymbol{\tau}_t | \boldsymbol{\tau}_{<t}, \mathcal{W}, \mathcal{I})}_{\text{trajectory gen}} \cdot \underbrace{\prod_t p(\mathbf{x}_t | \boldsymbol{\tau}_t, \mathcal{W})}_{\text{sensor simulation}}. \quad (1)$$

Next, we will discuss each individual task in detail.

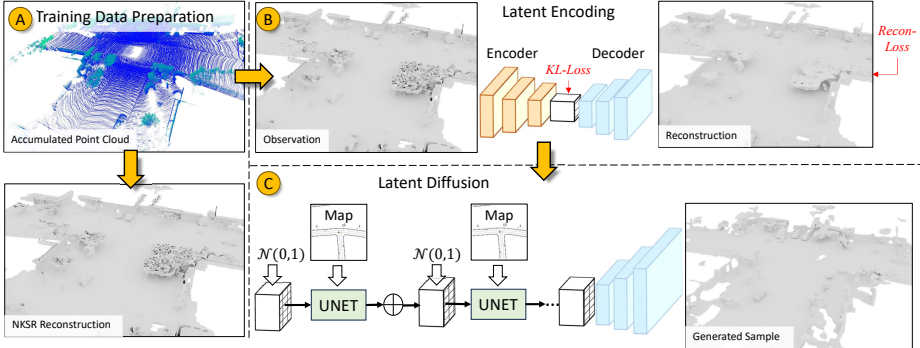


Fig. 4: Our 3D scene generation pipeline. First, accumulated point clouds are used to reconstruct each ground truth mesh sample. Next, a variational autoencoder is trained to compress meshes into a latent code. Finally, a map-conditioned diffusion model is trained to perform sampling within the latent space of the VAE, yielding novel samples.

3.2 Scene, Object and Trajectory Generation

We decompose the world into a static background scene, constant over time, and dynamic foreground objects that move. This decomposition simplifies the challenging 4D world generation into more manageable tasks: creating object geometries and generating dynamic effects. This modeling approach ensures temporal consistency (*e.g.* keeping cars’ shapes constant and walls and trees remain still over time) and physical plausibility (*e.g.* ensuring correct occlusion reasoning).

Scene Generation. The scene generation addresses the problem of sampling the geometry of a scene from a given input layout \mathcal{I} : $\mathbf{s} \sim p(\mathbf{s}|\mathcal{I})$. We parameterize the 3D scene using a signed distance field, $\mathbf{s} \in \mathbb{R}^{L \times W \times H}$, where each entry s_j encodes the truncated signed distance to the surface, $-1 \leq s_j \leq 1$, with negative values indicating outside the mesh and positive values inside the surface.

Model: We leverage the latent diffusion model [54, 54] to tackle this challenge of modeling and sampling from $p(\mathbf{s}|\mathcal{I})$. We choose the latent diffusion model for its capacity to sample high-quality data while effectively incorporating strong conditional guidance. Specifically, our model encodes the high-dimensional SDF volume \mathbf{s} into a continuous latent representation \mathbf{z} using an encoder-decoder structure [54] with a scene encoder $E_\theta(\mathbf{s}) = \mathbf{z}$ and a scene decoder $D_\theta(\mathbf{z}) = \tilde{\mathbf{s}}$. This encoder-decoder structure efficiently compresses the input data into a lower-dimensional latent space, enabling more effective and efficient sampling. Additionally, we encode our high-definition map layout \mathcal{I} into a latent space $\mathbf{c} = M_\theta(\mathcal{I})$, allowing for more compact conditioning.

Sampling: We leverage a probabilistic denoising diffusion model [54, 62] $F_\theta(\mathbf{z}, \mathbf{c})$ to perform classifier-free guidance sampling [23]. Specifically for each diffusion step k , the following Langevin dynamics step is performed to progressively de-noise until a clean sample \mathbf{z}_0 is acquired:

$$\mathbf{z}_{k-1} = \mathbf{z}_k + \frac{\lambda_k}{2} [(1+w)F_\theta(\mathbf{z}_k, \mathbf{c}) - wF_\theta(\mathbf{z}_k)] + \sqrt{\lambda_k}\epsilon_k$$

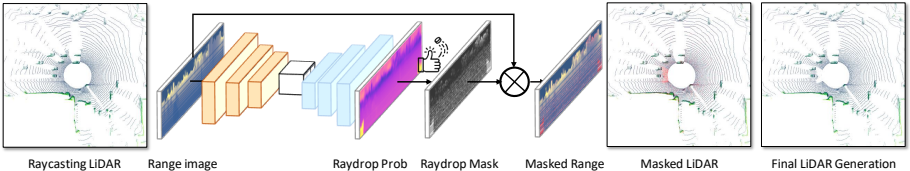


Fig. 5: Stochastic raydrop networks for sensory noise simulation, further enhancing realism. We highlighted the raydropped points in red on Masked Range and Masked LiDAR Images above.

$F_\theta(\mathbf{z}_k, \mathbf{c})$ is the score function $\nabla_{\mathbf{z}} \log p(\mathbf{z}|\mathbf{c})$ of the conditional distribution at \mathbf{z}_k and $F_\theta(\mathbf{z}_k, \mathbf{c} = \mathbf{0})$ is the the score function of the unconditional distribution $p_\theta(\mathbf{z})$. w is the CFG guidance scale parameter, λ_k is an annealed noise schedule parameter, and $\epsilon_k \sim \mathcal{N}(\mathbf{0}, \mathbf{I})$. Finally, a 3D scene sample \mathbf{s} is recovered by decode the reverse-diffused sampling latent code $\mathbf{s} = E_\theta(\mathbf{z}_0)$. Fig. 4(c) depicts the sampling procedure.

Training: We train our diffusion-based scene generation model using a dataset that pairs scene geometry with map conditioning. Direct access to dense scene geometry is not available in practice. Instead, we use the state-of-the-art dense geometry reconstruction approach, neural kernel surface reconstruction (NCSR) [28], to recover a pseudo-GT from an input LiDAR sequence. Ground truth annotations are used to remove moving dynamic objects, ensuring our reconstruction contains only the static scene and objects. We then train the auto-encoders for both scene geometry and map layout using reconstruction loss and KL divergence loss: $\min_\theta \mathcal{L}_{\text{recon}} + \mathcal{L}_{\text{KL}}$ over real-world examples (Fig. 4 (a)). Our latent diffusion model is trained using the score matching loss function: $\mathcal{L}_{\text{LDM}} = \mathbb{E}_{(\mathbf{z}, \mathbf{c}), \epsilon, k} [\|\epsilon - F_\theta(\mathbf{z}_k, k, \mathbf{c})\|_2^2]$, where \mathbf{z}_k is the forward diffused noisy sample at step k (Fig. 4 (b)).

Object Generation. Inspired by the rapid advancements in 3D shape generation, we employ two high-fidelity, 3D object generation frameworks, GET3D [19] and AvatarClip [26], to create dynamic traffic participants.

For each actor \mathbf{o}_i in a given layout \mathcal{I} , we sample a random variable $\mathbf{z} \sim \mathcal{N}$ and generate the corresponding actor mesh following $\mathbf{o}_i = G(\mathbf{z})$, where $G(\cdot)$ is the Generator/Decoder of the chosen generative method. For cars, trucks, and other four-wheeled vehicles, we use GET3D [19], which has demonstrated state-of-the-art and diverse generative results for 3D shapes, including cars. The layout box in \mathcal{I} is used to rescale the shape of each actor, ensuring that the sizes of the generated shape and the input layout are consistent. AvatarClip [26] is used to generate pedestrians conditioned on a SMPL [41] pose and shape parameter $\mathbf{p} = (\boldsymbol{\theta}, \boldsymbol{\beta})$. Furthermore, each generated rigged model is animated with a walking animation from Mixamo [3], ensuring a realistic 3D human walking motion sequence over time.

Together, the generated static world \mathbf{s} and each actor \mathbf{o}_i define our 3D world scenario, denoted as \mathcal{W} . Fig. 3 depicts the composed scene.

Trajectory Generation. To simulate a dynamic traffic scenario, we propose a retrieval-augmented generation coupled with a rejective sampling scheme to generate realistic and physically plausible dynamics for each actor and the ego vehicle, turning our 3D scene representation \mathcal{W} to 4D, denoting as \mathcal{W}_t for a given time t .

For the ego vehicle and each actor, jointly denoted as $\mathcal{P} = \{\tau_t\}$, we sampled trajectories from a trajectory bank obtained from Waymo Open dataset [63] and augment them to the scene. This guarantees realistic dynamics as the dataset is obtained from a diverse set of real-world scenarios. To ensure the physical feasibility of the sampled trajectories with respect to our generated scene, we reject those that violate rules of physics, such as collision with the static world, collision between actors, or hovering over the non-mesh area, while making sure to position them correctly above the ground. Around **12.3%** of sampled trajectories are retained. This rate is acceptable because resampling is trivial.

Additionally, for more realistic trajectory generation targeting for simulation use-cases, we extend Waymax [20], a data-driven 2D BEV traffic simulator, to control the behaviors of traffic actors in more systematic manners. Given a scenario from the WOMD Dataset [16], we use Waymax to replay ego-vehicle’s and agent’s real-world trajectories, with an additional reactive intelligent driving module [69] that updates each agent’s acceleration to avoid collisions. Since the trajectories are specific to the given real-world scenario, they are guaranteed to be physically plausible, but less diverse than our approach above.

Effectively, this approach renders our world generation to be completely asset-free, end-to-end generative, and thereby temporally consistent, allowing for a realistic, generative, and physics-based simulation without the need for artist-curated [14] or pre-collected assets [46, 74] as in previous lidar simulation method.

3.3 Physics-Informed LiDAR Generation

Given the complete 4D world \mathcal{W} and the poses \mathcal{P} , our next step is to generate a realistic LiDAR point cloud corresponding to these conditions. At a high level, we use the poses to compose the scene and objects at each timestep, then perform physics-informed ray casting to obtain purely physically simulated LiDAR as an intermediate result. As a final step, we leverage data-driven conditional sampling to generate the final LiDAR point cloud to simulate real-world LiDAR noises from the clean ray casting LiDAR.

Scene Composition. We use the Dual Marching Cube method [57] to obtain the 3D mesh of the static world from the generated TSDF volume \mathbf{s} . Then, with the trajectories of the ego car and all actors at time t , τ_t , we transform the 3D mesh to the world coordinates and compose it with \mathbf{s} , producing the full world geometry at each time t : $\mathcal{W}_t = \pi(\mathcal{W}, \tau_t)$ For each vehicle actor, π applies a rigid body transformation. For pedestrians, besides the rigid body movement, π additionally articulates the human body shape to simulate the animated nonrigid human movement with forward kinematics [7].

Physics-based Ray Casting. From the ego vehicle position τ_t , we perform ray-casting by utilizing Open3D [81] to compute ray-triangle intersections against the composed scene \mathcal{W}_t , obtaining the raycast scan $\bar{\mathbf{x}}_t$. To enhance realism of the raycasting to real-world LiDAR, we closely match the LiDAR sensor configuration (elevation angles, azimuth angles, field of view, etc.) with the real-world Lidar, depending on the use-case. For single-frame generation (Sec. 4.3), we follow the Velodyne HDL-64E manual [1] to match with KITTI-360 dataset [39]. For conditional multi-frame generation (Sec. 4.4), we use the calibration information provided with Waymo Open Dataset [63].

Stochastic Raydrop. Raycasted LiDAR from the generated world appears over-clean without real-world noises due to environmental and sensor noise factors. To address this, inspired by LiDARSim, we have an additional stage that stochastically simulates “raydrop”, where rays do not return to the sensor. For each raycast scan at time t , $\bar{\mathbf{x}}_t$, we project it onto a 2D spherical range image using polar coordinates. This image uses azimuth and zenith angles to represent coordinates and encodes depth values for each pixel. We predict raydrop probability per pixel on this image using a U-Net architecture [48] supervised by real-world LiDAR scan raydrop masks. Our approach, unlike LiDARSim, requires only a range map, eliminating the need for multiple additional metadata input channels that are only available in real-world data. We also apply a Gumbel sigmoid for random sampling. The application of our stochastic raydrop method produces the final LiDAR scan \mathbf{x}_t for each frame, concluding in our complete end-to-end LiDAR video generation process, as shown in Fig. 5.

4 Experiment

4.1 Setup

Datasets. We evaluate our proposed LidarDM on KITTI-360 [39] and Waymo Open [63] datasets. KITTI-360 is the de facto dataset for evaluating unconditional LiDAR generation methods. The dataset contains nine driving sequences (76,715 samples), where the first sequence is used as a val sequence (11,518 samples) and the last eight are used for training (65,197 samples). The sequences were collected across Karlsruhe, Germany with a 64 Beam LiDAR. However, KITTI-360 does not provide detailed BEV HD map information limiting its applications in conditional models. Waymo Open [63] is a dataset containing 1048 sequences with 158,000 training and 29,700 validation frames. A detailed HD map allows us to train conditional diffusion models. The HD map is in a vector format storing edges of map objects. We preprocess the map by centering it on each LiDAR Frame and rasterizing it into a segmentation map. The dimensions of the map tensor are $L \times W \times M$ (length \times width \times map classes). The map has 5 classes (lane markings, road lines, edges, crosswalks, driveways).

Training Details. We train our models using four Nvidia A100 40GB GPUs. We use the AdaM optimizer with a learning rate of 1e-4 for the VAE and 1e-5 for the diffusion U-Net, with a cosine decay schedule.

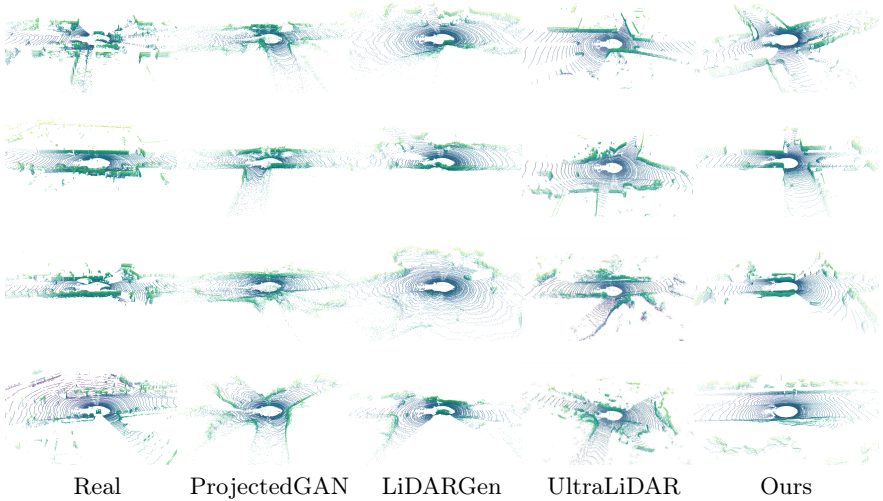


Fig. 6: Real KITTI-360 samples vs unconditional samples from the competing methods. UltraLiDAR sample visualizations are directly acquired from their paper. Compared to previous approaches, LidarDM generates samples that feature a greater quantity of more detailed salient objects (e.g., cars, pedestrians), sharper 3D structures (e.g., straight walls), and more realistic road layouts.

Model Details. The diffusion UNet, which is conditioned on layout and SDF latents, has 5 ResNet blocks with $2\times$ downsampling with channels of $\{128, 128, 256, 512, 512\}$. The SDF VAE has 4 ResNet blocks with channels of $\{448, 640, 896, 1280\}$. The Map VAE has ResNet down/upsample blocks with channels of $\{64, 64, 128, 256, 512\}$, and it is trained independently with X-Entropy and KL regularization.

4.2 Baselines

Unconditional Generation. LiDARVAE, LiDARGAN, ProjectedGAN, and LiDARGen are baselines that perform generation in the range image representation. UltraLiDAR performs generation in the BEV voxel space. To provide a fair comparison, we follow UltraLiDAR and evaluate MMD and JSD on a histogram of voxel occupancy instead of voxel density [72]. In addition, UltraLiDAR does not provide samples so we use their reported numbers in their original paper.

Temporal Coherency. We are the first to attempt the task of sequential LiDAR generation and thus no previous models exist for comparison. Nonetheless, we implement a sequence diffusion baseline inspired by recent work in video generation. We believe this approach is the most straightforward initial approach.

Concretely, we train a VAE to encode individual LiDAR frames. This has been shown previously [72] to be powerful and effective. Next, we train a diffusion model to directly denoise multiple (*i.e.*, 5) LiDAR frames at once. Visually, this approach yields decent temporal consistency.

Method	MMD _{BEV} (↓)	JSD _{BEV} (↓)
LiDAR VAE [8]	8.53×10^{-4}	0.267
LiDAR GAN [8]	8.95×10^{-4}	0.243
ProjectedGAN [56]	7.07×10^{-4}	0.201
LidarGen [83]	2.95×10^{-4}	0.136
UltraLidar [72]	9.67×10^{-5}	0.132
LidarDM (Ours)	1.67×10^{-4}	0.119

Table 1: Qualitative results for unconditional generation on KITTI-360 dataset. (■ best, □ second best, ■ third best)

Method	Total ICP Energy [m] (↓)	Average ICP Energy (↓)	Outlier Percentage (↓)	Chamfer Distance [m] (↓)
Sequence Diffusion	3616.58	0.078	20.56%	0.39
LidarDM (Ours)	916.94	0.014	7.12%	0.17

Table 2: Temporal consistency. Outlier percentage uses distance threshold $\tau = 0.5m$.

4.3 Unconditional Single-Frame Generation

We first validate our model architecture design and showcase our model’s generative capability by directly comparing against previous LiDAR generation models in unconditional generation on KITTI-360 [39].

Based on the results in Table 1, BEV models (such as ours or UltraLiDAR) perform best in top-down layout quality (as reflected by MMD and JSD) compared to range image models. The close performance gap compared to UltraLiDAR can be explained by the fact that UltraLiDAR was directly trained on the task of modeling single LiDAR scans which the benchmark evaluates. In addition, the BEV voxel grid representation offers large flexibility in generating physically implausible LiDAR readings that have the potential accurately match ground truth data in histogram metrics. We also show qualitative comparisons against the baselines in Fig. 6.

4.4 Map-conditioned Multi-Frame Generation

Our model is the first fully generative LiDAR model that can generate controllable (through map conditioning), realistic, and temporally coherent synthetic LiDAR scans. We will then validate these properties in this section.

Consistent Video Generation One of our key contributions is the temporal consistency of the sequential LiDAR generation. To evaluate this, we first use ICP alignment to calculate a relative transformation between consecutive generated frames. We then exploit LiDAR’s 3D nature and define an **average point-to-plane energy** over a sequence of LiDAR scans as our quantitative metrics, following this equation: $E = \frac{1}{T} \sum_{t=1}^T \text{point2plane}(x_t, x_{t-1})$ where `point2plane` represents the point-to-plane distance [42], and x_t indicates the

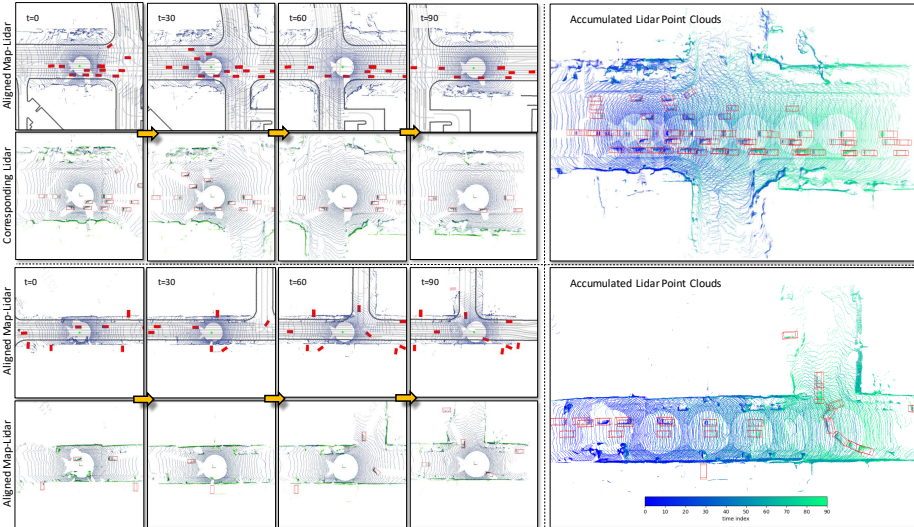


Fig. 7: Qualitative results of map-conditioned sequence generation on 2 Waymax [20] map sequences. We also showcase the corresponding accumulated point cloud to highlight the temporal consistency of LidarDM.

LiDAR scan at time t . Intuitively, E is prone to higher values from dynamic objects, but it is still a valuable metrics to determine if the general geometry of the 3D scene is preserved over time as the majority of the environment is static. To further evaluate the geometric consistency of the generative LiDAR sequence, we also measure the **outlier point ratio**, defined as the percentage of points with the `point2plane` distance larger than a certain threshold τ . Table 2 shows our quantitative results, where we beat the baseline in both metrics by a notable margin. These results clearly show that our LidarDM is capable of generating temporally-consistent LiDAR sequences.

	mAP (%)	mAP Agreement
Real	59.7	
LidarDM	56.4	81.1%

Table 3: Real2Sim: Detector [75] trained on real data can be evaluated on LidarDM-generated data, showing strong agreement with its real counterpart, suggesting its potential for simulation.

Layout-aware LiDAR Generation To ascertain the layout-awareness of our LidarDM, we use CenterPoint [75] trained on real-world LiDAR scans to validate whether it can accurately detect objects from the LidarDM’s LiDAR scan. As LidarDM currently does not generate intensity, we trained CenterPoint excluding intensity of the real-world LiDAR scans, hence the potential mismatch between our results and those obtained in the original paper [75].

Given an input layout \mathcal{I} , we generate the corresponding LiDAR scan, run CenterPoint on it, and evaluate using mean average precision (mAP) for vehicles.

Config	mAP (%)
35k Real	58.2
35k Real + 70k LidardM	61.3

Table 4: Data augmentation: LidarDM-generated data can enhance training for detectors on real-world data, suggesting its potential to improve the perception module without expensive data annotation.

We compare this result with the mAP from the raw LiDAR. The result in Table 3 indicates that CenterPoint’s object detection on our generated LiDAR scan is comparable to the ground truth. We also compute the mAP agreement between our generated LiDAR scan and raw LiDAR scan, indicating a strong agreement between the two and demonstrating our approach’s map-awareness and realism.

Qualitative results We show qualitative results of our map-conditioned LiDAR sequence generation in Fig. 7. Our generated results closely match the map conditioning by adding flat surfaces and static vehicles that correspond to the provided layout. The use of physical-based LiDAR sensor simulation guarantees that the generated point clouds are properly occluded by obstacles and appear as a realistic LiDAR sweep pattern. We also showcase the accumulated LiDAR points over 90 frames in Waymax [20], highlighting LidarDM’s temporal consistency and map-awareness.

4.5 Augmenting Real Data with LidarDM

LidarDM is the first LiDAR generative model capable of generating data conditioned on a given semantic layout. This capability offers the potential to augment the training data for 3D perception models, thereby further boosting their performance. To evaluate this capability, we first use LidarDM to generate around 70k frames of simulation data based on the layout from Waymo Dataset [63]. After that, we pre-train a LiDAR-based 3D object detection model, CenterPoint [75] (with PointPillars [36] as its backbone), on these generated LiDAR frames, paired with the object labels from the dataset. We then train the same model on 35k frames of real data, both with and without the pre-training stage on the simulation data, to test the benefits of the LidarDM-generated data. According to Table 4, LidarDM can act as an effective generative data augmentation strategy, offering more than a 3% improvement in detection accuracy.

5 Conclusion

In this paper, we introduced LidarDM, a novel layout-conditioned latent diffusion model for generating realistic LiDAR point clouds. Our approach frames the problem as a joint 4D world creation and sensory data generation task and develops a novel latent diffusion model to create 3D scenes. The resulting point cloud videos are realistic, coherent, and layout-aware.

Limitations So far, LidarDM relies on latent diffusion models, which are not real-time. Recent progress in latent consistency models promises to accelerate the generation process. We also leave LiDAR intensity modeling as future work.

Acknowledgement This project is supported by the NCSA Faculty Fellowship, and NSF Awards #2331878, #2340254, and #2312102 and gifts from Intel, IBM, Amazon, and Meta. We greatly appreciate the NCSA for providing computing resources. Vlas Zyrianov is supported by the New Frontiers Fellowship. The authors thank Scott Lathrop and Aaron D. Saxton for technical support with the NCSA Delta cluster.

References

1. High definitian lidar hdl-64e. <https://hypertech.co.il/wp-content/uploads/2015/12/HDL-64E-Data-Sheet.pdf>
2. Sketchfab. <https://sketchfab.com/feed>, accessed: 2021-11-26
3. Adobe Inc.: Mixamo. <https://www.mixamo.com/>
4. Afzal, A., Goues, C.L., Timperley, C.S.: Gzscenic: Automatic scene generation for gazebo simulator. arXiv preprint arXiv:2104.08625 (2021)
5. Ballé, J., Laparra, V., Simoncelli, E.P.: End-to-end optimized image compression. In: ICLR (2017)
6. Blattmann, A., Rombach, R., Ling, H., Dockhorn, T., Kim, S.W., Fidler, S., Kreis, K.: Align your latents: High-resolution video synthesis with latent diffusion models. In: CVPR (2023)
7. Bogo, F., Kanazawa, A., Lassner, C., Gehler, P., Romero, J., Black, M.J.: Keep it smpl: Automatic estimation of 3d human pose and shape from a single image. In: ECCV (2016)
8. Caccia, L., v. Hoof, H., Courville, A., Pineau, J.: Deep generative modeling of lidar data. In: IROS (2019)
9. Chang, H., Zhang, H., Jiang, L., Liu, C., Freeman, W.T.: Maskgit: Masked generative image transformer. In: CVPR (2022)
10. Chen, R., Chen, Y., Jiao, N., Jia, K.: Fantasia3d: Disentangling geometry and appearance for high-quality text-to-3d content creation. In: ICCV (2023)
11. Chen, Y., Rong, F., Duggal, S., Wang, S., Yan, X., Manivasagam, S., Xue, S., Yumer, E., Urtasun, R.: Geosim: Realistic video simulation via geometry-aware composition for self-driving. In: CVPR (2021)
12. Codevilla, F., Santana, E., López, A.M., Gaidon, A.: Exploring the limitations of behavior cloning for autonomous driving. ICCV (2019)
13. Dauner, D., Hallgarten, M., Geiger, A., Chitta, K.: Parting with misconceptions about learning-based vehicle motion planning. In: CoRL (2023)
14. Dosovitskiy, A., Ros, G., Codevilla, F., Lopez, A., Koltun, V.: CARLA: An open urban driving simulator. In: CoRL (2017)
15. Esser, P., Chiu, J., Atighehchian, P., Granskog, J., Germanidis, A.: Structure and content-guided video synthesis with diffusion models. In: ICCV (2023)
16. Ettinger, S., Cheng, S., Caine, B., Liu, C., Zhao, H., Pradhan, S., Chai, Y., Sapp, B., Qi, C., Zhou, Y., Yang, Z., Chouard, A., Sun, P., Ngiam, J., Vasudevan, V., McCauley, A., Shlens, J., Anguelov, D.: Large scale interactive motion forecasting for autonomous driving : The waymo open motion dataset. arXiv (2021)
17. Fang, J., Zhou, D., Yan, F., Zhao, T., Zhang, F., Ma, Y., Wang, L., Yang, R.: Augmented lidar simulator for autonomous driving. RAL (2020)
18. Feng, L., Li, Q., Peng, Z., Tan, S., Zhou, B.: Trafficgen: Learning to generate diverse and realistic traffic scenarios. In: ICRA (2023)

19. Gao, J., Shen, T., Wang, Z., Chen, W., Yin, K., Li, D., Litany, O., Gojcic, Z., Fidler, S.: Get3d: A generative model of high quality 3d textured shapes learned from images. In: Advances In Neural Information Processing Systems (2022)
20. Gulino, C., Fu, J., Luo, W., Tucker, G., Bronstein, E., Lu, Y., Harb, J., Pan, X., Wang, Y., Chen, X., Co-Reyes, J.D., Agarwal, R., Roelofs, R., Lu, Y., Montali, N., Mougin, P., Yang, Z., White, B., Faust, A., McAllister, R., Anguelov, D., Sapp, B.: Waymax: An accelerated, data-driven simulator for large-scale autonomous driving research. In: NeurIPS (2023)
21. Hahner, M., Sakaridis, C., Bijelic, M., Heide, F., Yu, F., Dai, D., Van Gool, L.: LiDAR Snowfall Simulation for Robust 3D Object Detection. In: CVPR (2022)
22. Harvey, W., Naderiparizi, S., Masrani, V., Weilbach, C., Wood, F.: Flexible diffusion modeling of long videos (2022)
23. Ho, J.: Classifier-free diffusion guidance. ArXiv (2022)
24. Ho, J., Jain, A., Abbeel, P.: Denoising diffusion probabilistic models. In: NeurIPS (2020)
25. Ho, J., Salimans, T., Gritsenko, A., Chan, W., Norouzi, M., Fleet, D.J.: Video diffusion models. arXiv:2204.03458 (2022)
26. Hong, F., Zhang, M., Pan, L., Cai, Z., Yang, L., Liu, Z.: Avatarclip: Zero-shot text-driven generation and animation of 3d avatars. ACM Transactions on Graphics (TOG) **41**(4), 1–19 (2022)
27. Hu, A., Russell, L., Yeo, H., Murez, Z., Fedoseev, G., Kendall, A., Shotton, J., Corrado, G.: Gaia-1: A generative world model for autonomous driving (2023)
28. Huang, J., Gojcic, Z., Atzmon, M., Litany, O., Fidler, S., Williams, F.: Neural kernel surface reconstruction. In: CVPR (2023)
29. Huang, L., Wang, S., Wong, K., Liu, J., Urtasun, R.: Octsqueeze: Octree-structured entropy model for lidar compression. In: CVPR (2020)
30. Huang, S., Gojcic, Z., Wang, Z., Williams, F., Kasten, Y., Fidler, S., Schindler, K., Litany, O.: Neural lidar fields for novel view synthesis. In: ICCV (2023)
31. Höppe, T., Mehrjou, A., Bauer, S., Nielsen, D., Dittadi, A.: Diffusion models for video prediction and infilling (2022), <https://arxiv.org/abs/2206.07696>
32. Karras, T., Aittala, M., Aila, T., Laine, S.: Elucidating the design space of diffusion-based generative models. In: Proc. NeurIPS (2022)
33. Karras, T., Laine, S., Aila, T.: A style-based generator architecture for generative adversarial networks. In: CVPR (2019)
34. Kim, S.W., Philion, J., Torralba, A., Fidler, S.: DriveGAN: Towards a Controllable High-Quality Neural Simulation. In: CVPR (2021)
35. Kim, S.W., Brown, B., Yin, K., Kreis, K., Schwarz, K., Li, D., Rombach, R., Torralba, A., Fidler, S.: Neuralfield-ldm: Scene generation with hierarchical latent diffusion models. In: CVPR (2023)
36. Lang, A.H., Vora, S., Caesar, H., Zhou, L., Yang, J., Beijbom, O.: Pointpillars: Fast encoders for object detection from point clouds (2019)
37. Ledig, C., Theis, L., Huszar, F., Caballero, J., Cunningham, A., Acosta, A., Aitken, A., Tejani, A., Totz, J., Wang, Z., Shi, W.: Photo-realistic single image super-resolution using a generative adversarial network. In: CVPR (2017)
38. Li, M., Zhou, P., Liu, J.W., Keppo, J., Lin, M., Yan, S., Xu, X.: Instant3d: Instant text-to-3d generation. arXiv preprint arXiv:2311.08403 (2023)
39. Liao, Y., Xie, J., Geiger, A.: KITTI-360: A novel dataset and benchmarks for urban scene understanding in 2d and 3d. PAMI (2022)
40. Liu, L., Ren, Y., Lin, Z., Zhao, Z.: Pseudo numerical methods for diffusion models on manifolds. In: ICLR (2022)

41. Loper, M., Mahmood, N., Romero, J., Pons-Moll, G., Black, M.J.: SMPL: A skinned multi-person linear model. *ACM Trans. Graphics (Proc. SIGGRAPH Asia)* **34**(6), 248:1–248:16 (Oct 2015)
42. Low, K.L.: Linear least-squares optimization for point-to-plane icp surface registration (01 2004)
43. Lu, C., Zhou, Y., Bao, F., Chen, J., Li, C., Zhu, J.: Dpm-solver: A fast ode solver for diffusion probabilistic model sampling in around 10 steps. In: NeurIPS (2022)
44. Luo, S., Tan, Y., Huang, L., Li, J., Zhao, H.: Latent consistency models: Synthesizing high-resolution images with few-step inference. arXiv preprint arXiv:2310.04378 (2023)
45. Macenski, S., Foote, T., Gerkey, B., Lalancette, C., Woodall, W.: Robot operating system 2: Design, architecture, and uses in the wild. *Science Robotics* (2022)
46. Manivasagam, S., Wang, S., Wong, K., Zeng, W., Sazanovich, M., Tan, S., Yang, B., Ma, W.C., Urtasun, R.: Lidarsim: Realistic lidar simulation by leveraging the real world. In: CVPR (2020)
47. Meng, C., He, Y., Song, Y., Song, J., Wu, J., Zhu, J.Y., Ermon, S.: SDEdit: Guided image synthesis and editing with stochastic differential equations. In: ICLR (2022)
48. Milioto, A., Vizzo, I., Behley, J., Stachniss, C.: RangeNet++: Fast and Accurate LiDAR Semantic Segmentation. In: IEEE/RSJ Intl. Conf. on Intelligent Robots and Systems (IROS) (2019)
49. Nakashima, K., Iwashita, Y., Kurazume, R.: Generative range imaging for learning scene priors of 3D lidar data. In: WACV (2023)
50. van den Oord, A., Vinyals, O., Kavukcuoglu, K.: Neural discrete representation learning (2018)
51. Podell, D., English, Z., Lacey, K., Blattmann, A., Dockhorn, T., Müller, J., Penna, J., Rombach, R.: Sdxl: Improving latent diffusion models for high-resolution image synthesis. arXiv preprint arXiv:2307.01952 (2023)
52. Poole, B., Jain, A., Barron, J.T., Mildenhall, B.: Dreamfusion: Text-to-3d using 2d diffusion. arXiv (2022)
53. Ramesh, A., Dhariwal, P., Nichol, A., Chu, C., Chen, M.: Hierarchical text-conditional image generation with clip latents. ArXiv (2022)
54. Rombach, R., Blattmann, A., Lorenz, D., Esser, P., Ommer, B.: High-resolution image synthesis with latent diffusion models. In: CVPR (2022)
55. Saharia, C., Chan, W., Saxena, S., Li, L., Whang, J., Denton, E.L., Ghasemipour, S.K.S., Ayan, B.K., Mahdavi, S.S., Lopes, R.G., Salimans, T., Ho, J., Fleet, D.J., Norouzi, M.: Photorealistic text-to-image diffusion models with deep language understanding. ArXiv (2022)
56. Sauer, A., Chitta, K., Müller, J., Geiger, A.: Projected gans converge faster. In: NeurIPS (2021)
57. Schaefer, S., Warren, J.: Dual marching cubes: primal contouring of dual grids. In: 12th Pacific Conference on Computer Graphics and Applications, 2004. PG 2004. Proceedings. pp. 70–76 (2004). <https://doi.org/10.1109/PCCGA.2004.1348336>
58. Schmidt, J., Khan, Q., Cremers, D.: LiDAR View Synthesis for Robust Vehicle Navigation Without Expert Labels. In: ITSC (2023)
59. Shah, S., Dey, D., Lovett, C., Kapoor, A.: Airsim: High-fidelity visual and physical simulation for autonomous vehicles. In: FSR (2017)
60. Shen, Y., Chandaka, B., Lin, Z.h., Zhai, A., Cui, H., Forsyth, D., Wang, S.: Simon-wheels: Physical world in the loop simulation for self-driving. arXiv preprint arXiv:2306.08807 (2023)
61. Song, J., Meng, C., Ermon, S.: Denoising diffusion implicit models. In: ICLR (2021)

62. Song, Y., Ermon, S.: Generative modeling by estimating gradients of the data distribution. In: NeurIPS (2019)
63. Sun, P., Kretzschmar, H., Dotiwalla, X., Chouard, A., Patnaik, V., Tsui, P., Guo, J., Zhou, Y., Chai, Y., Caine, B., Vasudevan, V., Han, W., Ngiam, J., Zhao, H., Timofeev, A., Ettinger, S., Krivokon, M., Gao, A., Joshi, A., Zhang, Y., Shlens, J., Chen, Z., Anguelov, D.: Scalability in perception for autonomous driving: Waymo open dataset. In: CVPR (2020)
64. Swerdfloor, A., Xu, R., Zhou, B.: Street-view image generation from a bird's-eye view layout. arXiv preprint arXiv:2301.04634 (2023)
65. Tallavajhula, A., Mericli, C., Kelly, A.: Off-road lidar simulation with data-driven terrain primitives. In: ICRA (2018)
66. Tan, S., Wong, K., Wang, S., Manivasagam, S., Ren, M., Urtasun, R.: Scenegen: Learning to generate realistic traffic scenes. CVPR (2021)
67. Tao, T., Gao, L., Wang, G., Lao, Y., Chen, P., Zhao, H., Hao, D., Liang, X., Salzmann, M., Yu, K.: Lidar-nerf: Novel lidar view synthesis via neural radiance fields (2023)
68. TechCrunch: Waveone aims to make video ai-native and turn streaming upside down. <https://techcrunch.com/2020/12/01/waveone-aims-to-make-video-ai-native-and-turn-streaming-upside-down/>, accessed: 2023-11-16
69. Treiber, M., Hennecke, A., Helbing, D.: Congested traffic states in empirical observations and microscopic simulations. Physical Review E **62**, 1805–1824 (02 2000). <https://doi.org/10.1103/PhysRevE.62.1805>
70. Villegas, R., Babaeizadeh, M., Kindermans, P.J., Moraldo, H., Zhang, H., Saffar, M.T., Castro, S., Kunze, J., Erhan, D.: Phenaki: Variable length video generation from open domain textual description. In: ICLR (2022)
71. Voleti, V., Jolicoeur-Martineau, A., Pal, C.: Mcvd: Masked conditional video diffusion for prediction, generation, and interpolation. In: NeurIPS (2022)
72. Xiong, Y., Ma, W.C., Wang, J., Urtasun, R.: Learning compact representations for lidar completion and generation. In: CVPR (2023)
73. Yang, R., Srivastava, P., Mandt, S.: Diffusion probabilistic modeling for video generation (2022)
74. Yang, Z., Chen, Y., Wang, J., Manivasagam, S., Ma, W.C., Yang, A.J., Urtasun, R.: Unisim: A neural closed-loop sensor simulator. In: CVPR (2023)
75. Yin, T., Zhou, X., Krähenbühl, P.: Center-based 3d object detection and tracking. CVPR (2021)
76. Yu, T., Xiao, T., Stone, A., Tompson, J., Brohan, A., Wang, S., Singh, J., Tan, C., Peralta, J., Ichter, B., et al.: Scaling robot learning with semantically imagined experience. In: RSS (2023)
77. Zeng, W., Luo, W., Suo, S., Sadat, A., Yang, B., Casas, S., Urtasun, R.: End-to-end interpretable neural motion planner (2021)
78. Zhai, J.T., Feng, Z., Du, J., Mao, Y., Liu, J.J., Tan, Z., Zhang, Y., Ye, X., Wang, J.: Rethinking the open-loop evaluation of end-to-end autonomous driving in nuscenes. arXiv preprint arXiv:2305.10430 (2023)
79. Zhang, L., Xiong, Y., Yang, Z., Casas, S., Hu, R., Urtasun, R.: Learning unsupervised world models for autonomous driving via discrete diffusion. arXiv preprint arXiv:2311.01017 (2023)
80. Zhang, L., Rao, A., Agrawala, M.: Adding conditional control to text-to-image diffusion models. In: ICCV (2023)
81. Zhou, Q.Y., Park, J., Koltun, V.: Open3D: A modern library for 3D data processing. arXiv:1801.09847 (2018)

82. Zhu, X., Zyrianov, V., Liu, Z., Wang, S.: Mapprior: Bird's-eye view perception with generative models (2023)
83. Zyrianov, V., Zhu, X., Wang, S.: Learning to generate realistic lidar point cloud. In: ECCV (2022)

LidarDM: Generative LiDAR Simulation in a Generated World – Supplementary Materials

Abstract. In the following supplementary material, we provide additional model details and ablations (Sec. 1). In Sec. 2 we provide additional qualitative LidarDM results, including a baseline comparison, a close look at pedestrian details, and visualizations of map condition alignment. In Sec. 3, we provide additional downstream applications such as crafting safety-critical and out-of-distribution scenarios for self driving. In Sec. 3.3, we perform a Sim2Real data augmentation experiment on an end-to-end LiDAR-based planner.

1 Experimental Details

1.1 Sequence Diffusion Baseline.

The sequential diffusion baseline follows a latent diffusion architecture similar to that of LidarDM. However, it uniquely adopts a BEV LiDAR representation, encoding the observed voxelized point cloud, in line with advanced LiDAR generation methods. This approach specifically employs a binary occupancy grid centered around the ego sensor [72]. The training process is conducted in two stages. Initially, a VAE is trained using cross-entropy for reconstruction loss on this data, supplemented by KL divergence regularization. In practice, we found Ultralidar’s discrete code does not perform as well as continuous latent space. Following this, a diffusion model is trained in the latent code space. This model is conditional and its training mirrors that of LidarDM; it utilizes the same map latent code, which is occasionally omitted during training (20% of the time) [23]. For consistent generation, the model simultaneously denoises five latent codes, each corresponding to a LiDAR frame, through a latent code-concatenation technique. This baseline is developed on four Nvidia A100 40GB GPUs. The AdaM optimizer is used, with a learning rate of 1e-4 for the VAE and 1e-5 for the diffusion U-Net, following a cosine decay schedule.

This setup allows for an effective comparison between the baseline and our approach, demonstrating the efficacy of the core idea of jointly generating a 4D world during sensor generation.

1.2 Raydrop Ablation

We perform an ablation study on various ray-dropping options in Table 1. The table suggests that Gumbel Softmax generally yields better-calibrated LiDAR ray drops than Softmax (the one used in Lidarsim), with lower JSD and MMD. Additionally, although not using ray dropping yields a decent MMD score, it

significantly increases the number of points (doubling the ground truth number of points), making it unrealistic. For a fair comparison, all configurations are evaluated on the same subset of underlying validation 3D worlds (hence the numbers might slightly differ from our reported test numbers).

Config	MMD _{BEV} (\downarrow)	JSD _{BEV} (\downarrow)
No Raydrop	1.730×10^{-4}	0.1286
Softmax	1.990×10^{-4}	0.1274
Gumbel (Ours)	1.846×10^{-4}	0.1271

Table 1: Raydrop Ablation. (█ best, █ second best, █ third best)

2 LidarDM Additional Results

2.1 Sequential Diffusion Comparison.

We compare the layout-conditioned LiDAR video generation results of our method with the strong sequential diffusion baseline, as described in Section 4.2 of the main paper. Fig. 1 displays these results. From these, it is evident that our approach significantly outperforms the baseline in terms of realism and layout-awareness. Specifically, we would like the readers to pay attention to the dynamic object's shape, the layout of walls and other static infrastructures, and missing objects in the baseline.

2.2 Pedestrian Motion.

Thanks to actor insertion, we can accurately model fine details such as walking pedestrians compared to other pure generative results. Fig. 3 visualizes such case, offering a view in both how the underlying pedestrian meshes behave, as well as how the corresponding LiDAR points are affected.

2.3 More Map-aligned Qualitative Results.

Fig. 2 presents more map-aligned visualization as well as accumulated point cloud, ensuring the map-awareness and temporal consistency of our approach. We encourage the readers to watch our supplementary videos for better visualization of qualitative results. **Note:** the black lines on the map indicates the road edge (which corresponds to a "bump" in LiDAR data as indicated in the color boxes), not structures (buildings, walls). Thus, our LiDAR points end outside of those black edges (which corresponds to structures, such as buildings). This is consistent with the real-world LiDAR.

3 LidarDM Downstream Tasks Results

3.1 Safety-Critical Scenarios

We argue that one of the many benefits of LidarDM is the ability to extend existing traffic simulators with realistic and scenario-aware LiDAR data, allowing for sensor-based critical safety scenario evaluation of autonomous system. More specifically, we extend Waymax [20], a BEV traffic simulator, and showcase how LidarDM can create realistic LiDAR for two types of safety-critical scenarios, *ego-vehicle behavior manipulation* (Fig. 4) and *actors behavior manipulation* (Fig. 5).

3.2 Out of Distribution Object Insertion

We demonstrate the strong controllability and flexible nature of our generative approach by replicating dangerous scenarios in simulation. Similar to our approach on vehicle or pedestrian actors (Sec. 3.2), we obtain the out-of-distribution meshes from generative models (or even off-the-shelf assets on Sketchfab [2]). For trajectories, we find it sufficient to sample from vehicles’ trajectories from the trajectory bank, or simply pre-define a series of road-crossing trajectories. In Fig. 6, we show an example of inserting dangerous animals into the scene. These scenarios are not present in the Waymo dataset [63], but may occur in real life due to escaped zoo animals or on roads that are near wildlife habitats.

3.3 LidarDM as Data Augmentation for Planning

Inspired by our perception data augmentation experiment, we performed a second Sim2Real experiment to demonstrate that LidarDM-generated data can aid in training a learning-based end-to-end motion planner. **Model and inference:** Drawing inspiration from the Neural Motion Planner [77], we developed a learning-based motion planner that takes the five most recent LiDAR observations (covering 0.5 seconds of past history) as input and generates a dense cost map of size $W \times H \times T$ for the future, where T represents the number of future timestamps. In this case, $T = 10$, with a 0.3-second interval between consecutive frames. During inference, we sample trajectories from a trajectory bank and select the one with the lowest overall cost as the final planned trajectory. **Training:** During training, we employ a soft cross-entropy loss to train the cost map and generate a trajectory bank from the Waymo dataset using K-Means. Training and validation is done following the standard splits on Waymo Open dataset. **Remark:** We want to highlight two key differences compared to the vanilla NMP model: 1) our motion planner does not require privileged HD Maps as input, and 2) the motion planner does not explicitly incorporate the ego car’s past trajectory. The first design choice ensures that the model focuses on leveraging sensor data; hence, the comparison concentrates on evaluating the quality of our generated LiDAR point clouds. The second choice is inspired by recommended practices and findings from recent studies [12, 13, 78], suggesting

that incorporating ego vehicle’s past states results in short-cut effects and biases imitation learning for end-to-end driving.

Experimental details: In order to show that LidarDM-generated data can help augment the motion planner, we first train a model on 92k snippets of LidarDM-generated sequences, then fine-tune it on 9.2k real data sequences. Note that we use trajectories of expert drivers as GT and use traffic layout conditions to generate our LidarDM samples. As a comparison, we also train the same planner model using only the 9.2k real data sequences. To ensure fairness, we train both the real-only model and the real+sim model for a total of 30 epochs until convergence and choose the best model based on minimal validation loss.

Experimental results: We report two metrics: 1) the collision rate at a 3-second future, which measures the safety and traffic awareness of the planner; and 2) the L2 distance at 1 second, 2 seconds, and 3 seconds, which measures the accuracy for imitation. We present our results in Table 2. Using generative pre-training improves the performance of the planner in a low-data regime. In particular, our collision rate after 3 seconds has been reduced by 32% (relative) from 1.65% to 1.12%. To our knowledge, this is the first time conditional LiDAR generation has been shown to improve an end-to-end motion planner.

Config	L2 (m) @ 1.0s	L2 (m) @ 2.0s	L2 (m) @ 3.0s	Collision Rate (%)
9.2k Real	0.489	1.374	3.279	1.65%
9.2k Real + 92k LidarDM	0.490	1.341	3.160	1.12%

Table 2: Planner data augmentation: LidarDM-generated data can enhance the training of a Neural Motion Planner [77]-inspired model on real-world data, suggesting its potential to improve the planning module without expensive data collection. (■ best, ■ second best)

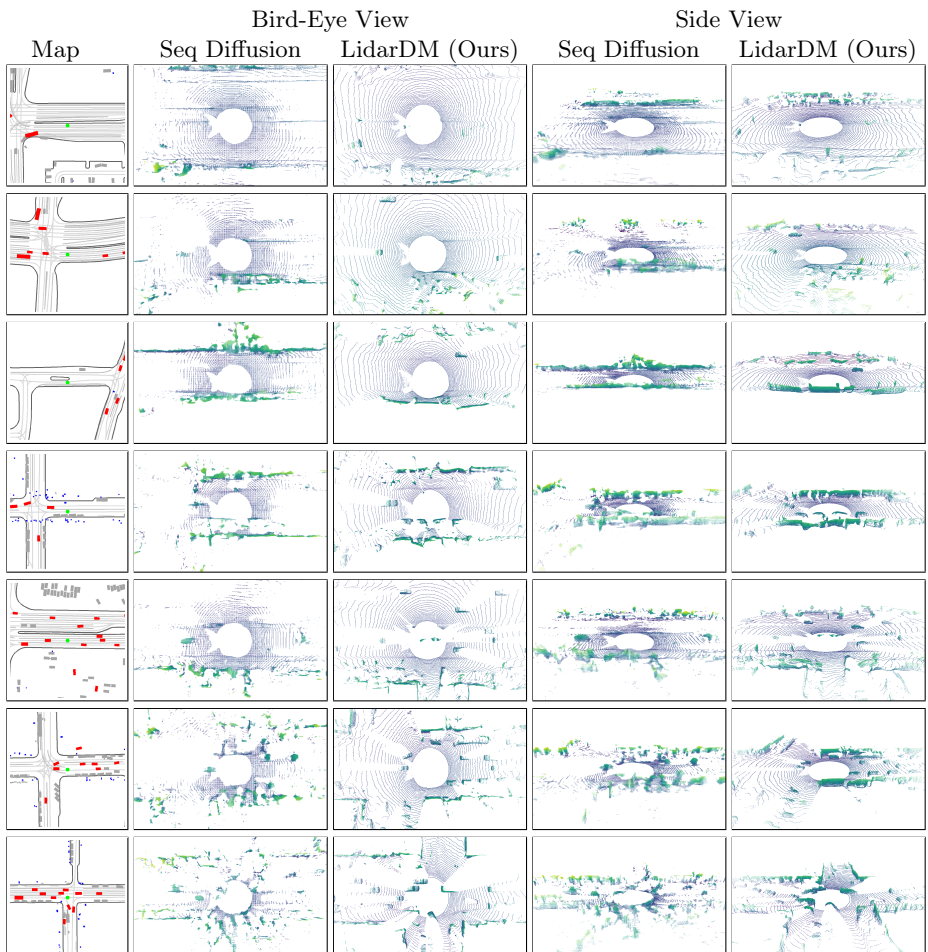


Fig. 1: Comparison of Layout-Conditioned LiDAR Generation on Waymo dataset: Our approach significantly outperforms the strong latent-diffusion-based sequential generation baseline in terms of realism, physics plausibility, and coherence with the input layout.

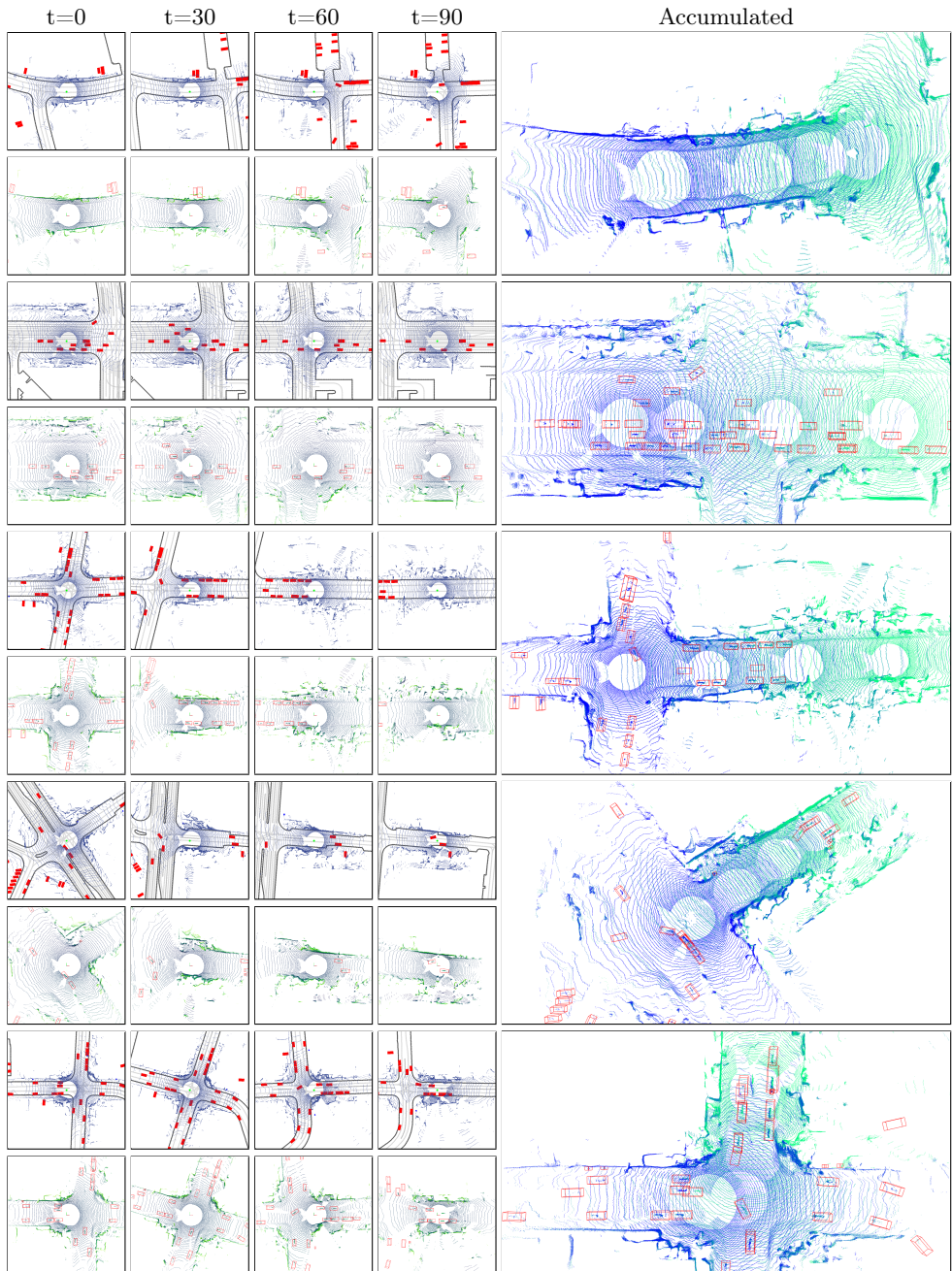


Fig. 2: More Map-Aligned Qualitative Results. We showcase 4 different frames of the same sequence, with both map-aligned and LiDAR top-down view. We also show the accumulated point clouds, colored by their time index to showcase the temporal consistency.

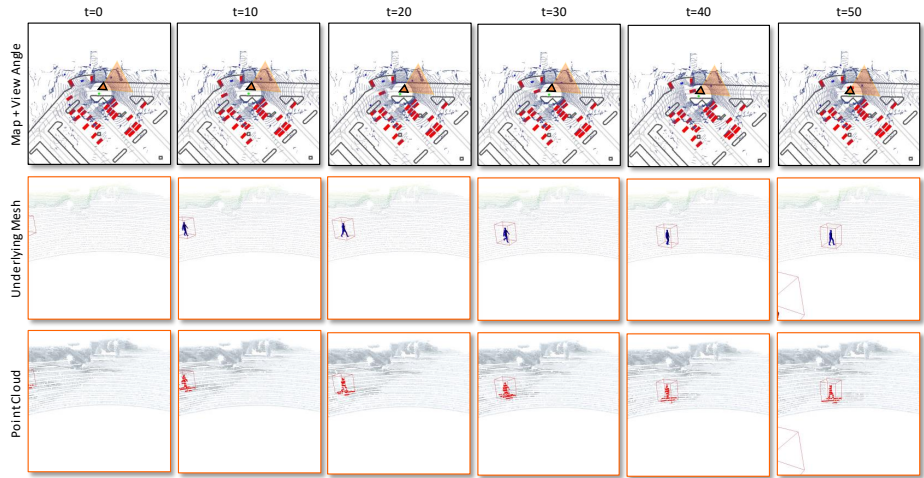


Fig. 3: Pedestrian motion captured with LidarDM: Thanks to our actor insertion approach, we can capture high-fidelity pedestrian movement through LiDAR, which none other generative method can achieve.

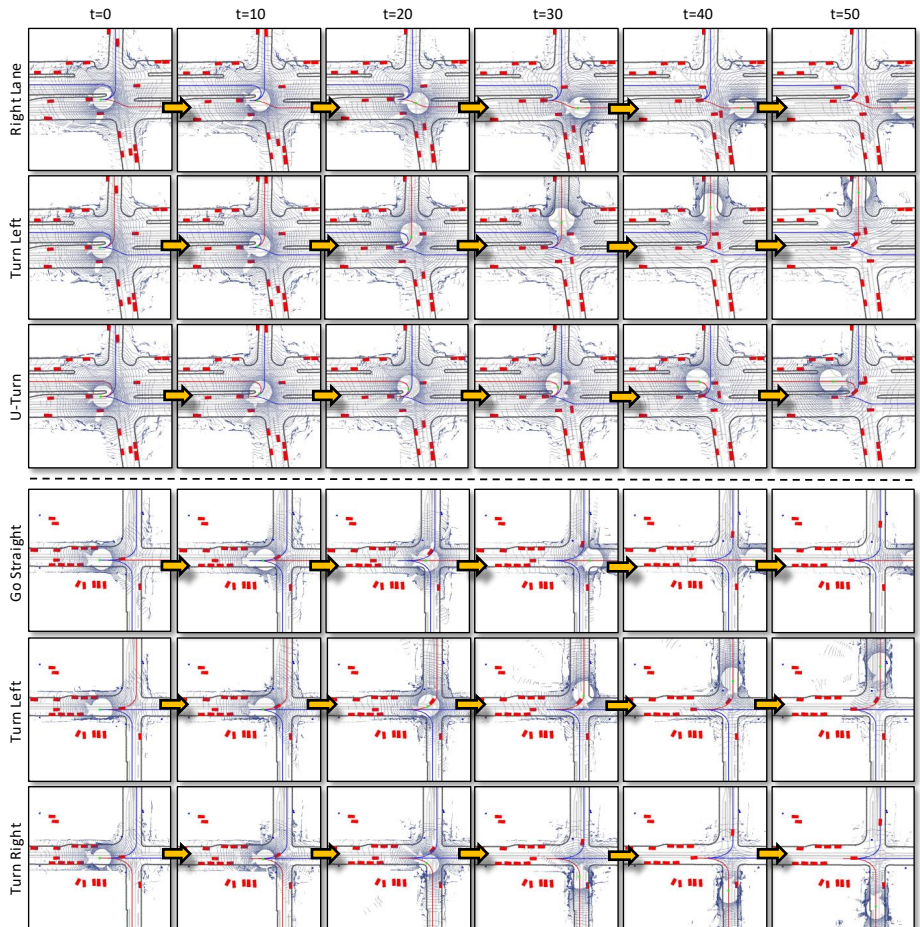


Fig. 4: Ego-Vehicle Behavior Manipulation: By extending Waymax, we can perform safety-critical scenarios evaluation of autonomous system. We showcase that LidarDM can produce realistic LiDAR for different simulated ego trajectories from 2 Waymax sequences.

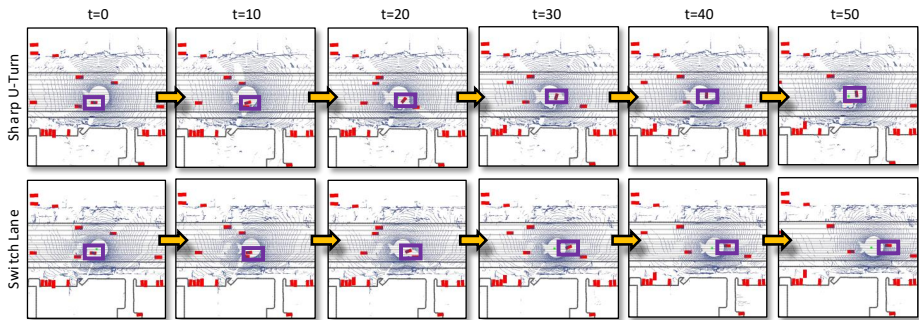


Fig. 5: Actor Behavior Manipulation: To create challenging situation that constitute a safety-critical scenario, we showcase that LidarDM can also produce realistic LiDAR data for when the actor’s behavior is manipulated, as indicated in the purple boxes.

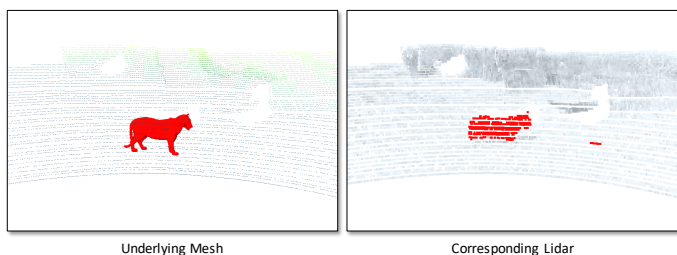


Fig. 6: Rare Scenario Simulation: The provided LidarDM approach is grounded in physical simulation, suggesting that our generative method can be combined with standard physics-based ray casting simulation to simulate out-of-distribution rare cases, such as a tiger crossing the street.